

Phase diagram of solid hints new fundamental constant and sees atomic orbital

Shapiullah Belalovich Abdulvagidov (✉ abdulvagidovshb@gmail.com)

Research Article

Keywords: phase diagram, hysteresis, diamond, enormous pressure, solid-state tomography, core of star, fundamental constants, transition temperature, phase boundary, transition-metal oxides, organic superconductor, manganite

Posted Date: December 1st, 2021

DOI: <https://doi.org/10.21203/rs.3.rs-1114543/v1>

License:  This work is licensed under a Creative Commons Attribution 4.0 International License.

[Read Full License](#)

Phase diagram of solid hints new fundamental constant and sees atomic orbital

Shapiullah Belalovich Abdulvagidov

Institute of Physics, Dagestan Federal Research Centre of RAS, Makhachkala, Republic of Dagestan

Email: abdulvagidovshb@gmail.com

Cold and pressure transform gas into liquid and then into solid. Van der Waals understood the phase diagram of liquefiable gas with the molecular volume and intermolecular attraction, however, was silent on how solid behaved¹. Unfortunately, solid-state phase diagram have remained uncomprehended mystery; only its straight boundary^{2,3} was explained by struggle of order vs. chaos. Here we show that the volume of orbital overlap has its own energy, with the universal density $8.941 \text{ eV}/\text{\AA}^3$ announced as new fundamental atomic constant that determines the transition temperature T_C . Furthermore, we devised solid-state tomography, valid to 5 TPa, - imaging orbital through the baric dependencies of T_C . Triangle-shaped pattern of the diagram is explained by the only possible way, just as only one plane passes through triangle: -inflation of the intersection volume during the transition determines hysteresis, but its disappearance does triple point; -approaching ions, whose orbitals overlap, curves the line from zero-field-cooling (ZFC) T_C to triple point; -the straight line between zero-field-heating (ZFH) T_C and triple point is a consequence of straightening tilting angle. Diamond melting point, calculated from volumes of the tetrahedral covalent bonds, excellently agrees with real; furthermore, the points up to 2 TPa agree with experiment⁴. Our findings open up way to interpret antiferromagnetism and steric effect in mono, binary, and ternary transition-metal oxides and sulfides⁵⁻¹¹, and advance in unravelling unconventional superconductivity^{12,13}, ascertaining the roles of σ - and π -hybridizations. Thereby, the importance of the solid-state tomography for organic conductors^{12,13} being high-compressible and interior of stars can scarcely be exaggerated.

In 1873, Van der Waals showed that the volume of molecules of the gas has the matter and they interact between them with the force named later in his honour¹, however, was silent on how solid behaves. Van der Waals' studies allowed Kamerlingh Onnes¹⁴ to liquefy helium and discover superconductivity in mercury; so unravelling the mystery of phase chart of gas had advanced not only physics of gas and liquid, but also solid. Solid is the last aggregate state of substance, which only changes its structural, electronic, magnetic and other properties till either its temperature has become infinitely close to absolute zero or its destruction under enormous temperature and pressure in the core of star. Unfortunately, up to now the phase chart of solid capable to advance science remains an uncomprehended mystery. Boundaries between the different properties of solid often behave intriguing manner. The phase charts of organic and cuprate superconductors where four different states meet at the multicritical point¹² is especially interesting. The phase diagram of iron no less attractive puts up, however, knotty issue about whether the number of solid phases should be raised to five¹⁵. This work reveals the nature of the phase diagram of solid, that is, answers the question been silent by Van der Waals.

We have asked ourselves why the phase boundaries of $\text{Sm}_{0.55}\text{Sr}_{0.45}\text{MnO}_3$ manganite behave straightly with different slopes along the lines BC and DE and curvedly on AC (Fig. 1). The DE line energy slope $\frac{k_B \Delta T_C / \Delta B}{\mu} = 0.99$ [Hund's rule gives $\mu = 6\mu_B$ both for Mn^{+3} and for Mn^{+4} (Supplementary Table S1)] means that magnetic field only suppresses the thermal agitation and so the Curie point is linear:

$$T_C = \frac{\mu}{k_B} B \cos\theta. \quad (1)$$

The $\widehat{\mu \cdot B}$ angle θ is, at the same time, a tilting one between the adjacent $\text{Mn}^{+3}\text{O}_6^{-2}$ and $\text{Mn}^{+4}\text{O}_6^{-2}$ octahedrons; along DE $\theta_{DE} = \arccos 0.99 = 8.2^\circ$.

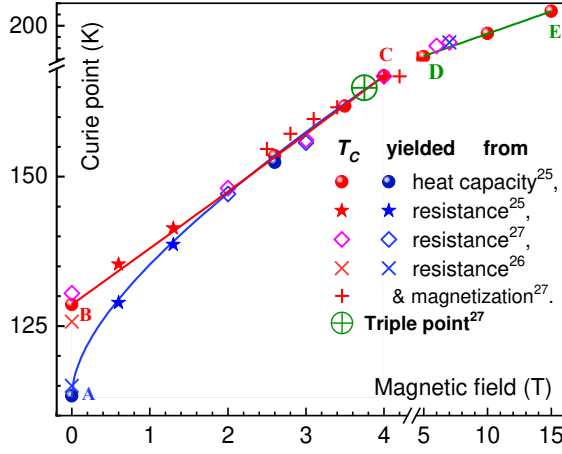


Fig. 1. | The Curie-point-magnetic-field diagram [$T_C(B)$] of $\text{Sm}_{0.55}\text{Sr}_{0.45}\text{MnO}_3$.

Ferromagnetism appears at downward and/or rightward crossing of the curve AC but disappears at upward and/or leftward crossing of the line BC . So if the triangle-like region ABC has been reached from under AC (above BC) it is ferromagnetic (paramagnetic), that is, the nonvolatile memory effect driven both by temperature and by magnetic field takes place. AC , BC and DE are seen to excellently describe the Curie points (the red signs at heating and the blue at cooling) both of polycrystalline^{25,26} and of single crystal²⁷.

Our attempts to interpret the steep energetic pitch 2.37 of BC as easy as DE failed. To reveal the secret of BC was previously necessary to explain AC . We supposed that the transition temperature T_{tr} is proportional to the volume of the double spheric cap $V = 2\pi h^2(R - h/3)$ formed at the intersection height h of two orbitals with the radius R of their spheric ends (Fig. 2a). So the intersection volume has the energy that equals the phase-transition energy $k_B T_{tr}$. By introducing the energy density v ,

$$T_{tr} = \frac{2\pi v}{k_B} h^2(R - h/3). \quad (2)$$

The subscript tr points out that Exp. (2) suited for different-type transitions - Curie, Neel, Mott and melting points. The indirect intersection of half-filled orbital with empty through full-filled (that is, diamagnetic) orbital leads to double exchange, but with half-filled to superexchange which, in turn, forbids the Mott's conductance. The direct intersection of half-filled orbitals creates covalent bond whose energy and number yield the melting point.

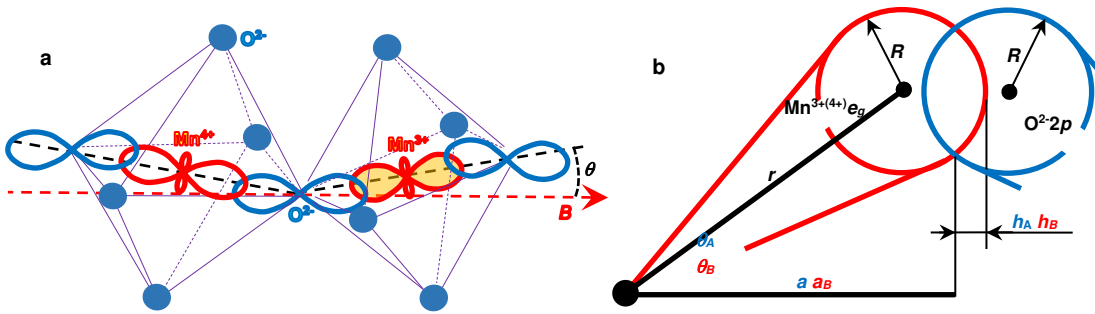


Fig. 2. | The biconvex-lens volume of the orbital intersection and the geometric calculation of the intersection height h_B . **a.** The tilting angle θ between MnO_6 octahedrons and magnetic field B determines the $\text{Mn}^{3+(4+)}$ magnetostatic energy $6\mu_B \cos\theta$. **b.** The blue letterings belonging to the point A yield the distance r from the site $\text{Mn}^{3+(4+)}$ or O^{2-} to the center of the curvature R of the spheric end of its e_g or $2p$ orbital, $r = (a - R + h_A) / \cos\theta_A$. The red letterings belonging to the point B give $h_B = r \cos\theta_B - a_B + R$, which with the r calculated from the blue letterings, transforms into Exp. (4).

Obviously, the intersection height $h = \epsilon a$, a is half a distance between $\text{Mn}^{3+(4+)}$ and O^{2-} and ϵ a relative striction. A magnetic cation shrinking solid wastes its magnetostatic energy on enhancing the elastic energy of unit-cell volume V : $\mu \cdot \mathbf{B} = VE\epsilon^2/2$, E is Young's modulus. Then $\epsilon = \sqrt{2\mu \cdot \mathbf{B} / VE}$ and so $h = a\sqrt{2\mu \cdot \mathbf{B} / VE}$, as ZFC Curie point T_C^A is nonzero, it needs to add the threshold intersection height h_A to this. Substitution of $h = a\sqrt{2\mu \cdot \mathbf{B} / VE} + h_A$ into Exp. (2) gives

$$T_C = \frac{2\pi v}{k_B} \left(\frac{2a^2\mu \cdot \mathbf{B}}{VE} + 2h_A a \sqrt{\frac{2\mu \cdot \mathbf{B}}{VE}} + h_A^2 \right) \left[R - \left(a \sqrt{\frac{2\mu \cdot \mathbf{B}}{VE}} + h_A \right) / 3 \right]. \quad (3)$$

Magnetic field supports magnetism along AC same as on DE , therefore, the best physical description of AC is the sum of Exps. (3) and (1) at $\cos\theta$ linearly turning down from θ_A to $\theta_C \cong \theta_{DE}$ ($\cos\theta$ linearly depends both on temperature¹⁶ and on the rare-earth-cation radius¹⁷, therefore to preset its magnetic-field linearity is quite reasonable). We found the best fit with the root-mean-square error (RMSE) 0.58 K at the initial and fitted quantities mentioned in Table 1. So the curvilinearity of AC is a consequence of the curvilinear field dependence of the intersection volume at the striction, that is, approaching $\text{Mn}^{3+(4+)}$ and O^{2-} in the paramagnetic state just before appearing the ferromagnetism.

To understand hysteresis AB is to know why the ZFH Curie point T_C^B is higher than T_C^A . We think that h_A triggers double exchange, which removes the Coulomb distortion¹⁸ (certainly the chemical distortion, defined by the tolerance factor, remains), the orbital overlap inflating till h_B . The geometric constructions (Fig. 2b) for the points A and B give

$$h_B = (a - R + h_A) \cos\theta_B / \cos\theta_A - a_B + R, \quad (4)$$

a_B is half a distance between $\text{Mn}^{3+(4+)}$ and O^{2-} at B . Expression (2) with $h = h_B$ and the entries for B (Table 1) gives $T_C^B = 130.07$ K excellently consistent with the experimental 128.6 K. Thus, at T_C^A , h_A avalanche-like widens till h_B which generates T_C^B observable at heating only. Thus, the mystery of hysteresis is due to the changing of intersection volumes during the type-I-like transition, that is, $T_C^B - T_C^A = \frac{2\pi v}{k_B} [h_B^2(R - h_B/3) - h_A^2(R - h_A/3)]$.

Now we are able to interpret BC wherein magnetic field, straightening θ from θ_B to θ_C same as AC (otherwise the triple point is not), orientates the MnO_6 octahedrons, the intersection expanding. As θ does not change the spacing $\text{Mn}^{3+(4+)}\text{-O}^{2-}$, Exp. (4) transforms into

$$h_{BC} = (a_B - R + h_B) \cos\theta(B) / \cos\theta_B - a_B + R. \quad (5)$$

Magnetic field supports magnetism on BC same as on AC and DE because the best graph of BC is also a sum of Exp. (2) with $h = h_{BC}$ and Exp. (1). BC excellently traces the data with RMSE 1.37 K only with the initial entries, without fitting (Table 1). So the linearity of BC is a consequence of the linear field dependence of the intersection volume at straightening $\theta(B)$ in ferromagnetic state.

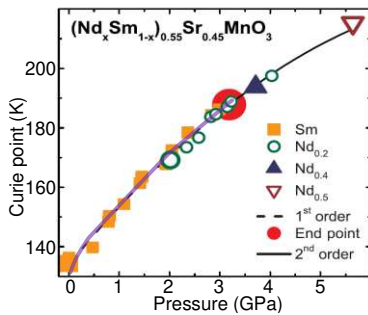


Fig. 3. | $T_C(P)$ diagram²⁷ fitted by Exp. (6) (the translucent purple curve) with $E(P) = 325P^{1/3} + E_0$.

In the case of the pressure diagram, the Hooke law $P = E(P)\varepsilon$ (the Young's modulus $E(P)$ is supposed to depend on pressure as well as temperature¹⁹, magnetic order²⁰ and even form²¹) gives $h = aP/E(P) + h_B$ which turns Exp. (2) into

$$T_{tr} = \frac{2\pi v}{k_B} \left(\frac{a^2 P^2}{E(P)^2} + 2h_B \frac{aP}{E(P)} + h_B^2 \right) \left[R - \left(\frac{aP}{E(P)} + h_B \right) / 3 \right]. \quad (6)$$

Expression (6) with the initial entries (Table 1) and only with fitting the prefactor and power in $E(P) = 325P^{1/3} + E_0$ excellently fits the $T_c(P)$ diagram¹⁸ in $(\text{Sm}_{1-x}\text{Nd}_x)_{0.55}\text{Sr}_{0.45}\text{MnO}_3$ (Fig. 3).

Finally, our calculation of the diamond melting-point is the brightest approbation of our discovery. Diamond starts to melt when its atom receives the energy enough to break all its covalent bonds. The diamond sp^3 -orbitals intersection is the carbon p -orbital length minus the diamond covalent radius²²: $h = r_p - r_c$, where r_p is obtained as the carbon-hydrogen distance in methane ("gaseous diamond") plus the hydrogen covalent radius and minus Bohr radius: $r_p = r_{\text{CH}_4} + r_{\text{H}_2}^c - r_B$. Expression (2) multiplied by the four covalent bonds with this h and $R=r_p/4$ gives the diamond melting point 4157°C in excellent agreement with the real 4000°C (Supplementary Table S1). To further affirm our theory, proceeding from the warrantable assumption that the diamond phase persists under enormous pressure²³, we calculated the baric dependence of the melting-point in diamond, $T_{tr}(P)$, through its $\rho(P)$ taken from Extended Data Table²⁴ 1. The baric dependence of the covalent radius

$$r_c(P) = \frac{\sqrt{3}}{8} \left(\frac{8 \cdot 12 m_u}{\rho(P)} \right)^{1/3}, \quad (7)$$

m_u is the atomic mass constant. Then $h(P) = r_p - \frac{\sqrt{3}}{8} \left(\frac{8 \cdot 12 m_u}{\rho(P)} \right)^{1/3}$ and $T_{tr}(P) = \frac{2\pi v r^2}{3k_B R^2} h^2(P) [3R - h(P)] + \Delta T_{tr}(P)$, calculated for the ellipsoidal intersection (r and R are the large and small semiaxes). $\Delta T_{tr}(P) = P \frac{12m_u}{k_B} \left[\frac{1}{\rho(0)} - \frac{1}{\rho(P)} \right]$ is the pressure-induced contribution resembling the energy of ideal gas $U = PdV$, where $U = k_B \Delta T_{tr}(P)$ and $dV = 12m_u [1/\rho(0) - 1/\rho(P)]$ is the striction of the unit cell per a carbon, and analogous to the magnetostatic addition of Exp. (1); that is, both pressure and magnetic field in themselves increase T_{tr} . Our calculated $T_{tr}(P)$ are quite satisfactory with the experiment⁴ (Fig. 4a).

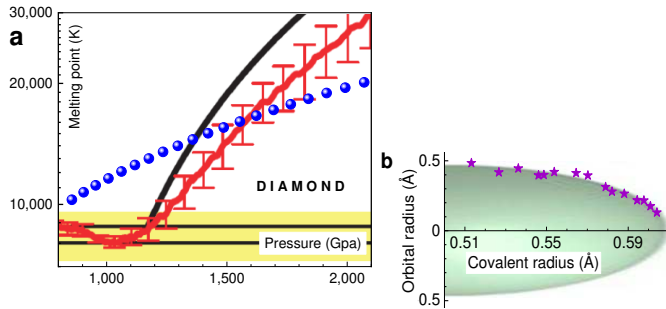


Fig. 4. | The melting point of diamond up to 2000 GPa and tomography of its sp^3 orbital up to 5000 GPa. a. The background is the cutting from the inset of Fig⁴. 4; red line shows the measurements⁴ and black line the values⁴ calculated assuming a constant specific heat. Blue balls mark our data; the uncertainties are smaller than the symbol size. The values of our graph are quite satisfactory with the lines⁴, but its go does not with. That is, the ellipsoidal shape of the orbital does not work at extremal pressure and realistic fits are necessary. $T_{tr}(P) = \frac{16\pi v}{k_B} \int_0^P R^2(r_c) \partial r_c(P)$, derived from Exp (8), gives a possibility to precisely describe $T_{tr}(P)$ provided $r_c(P)$ and $R(r_c)$ are known from other experiments. **b.** Solid-state tomography (pink stars) of sp^3 -orbital in diamond, obtained from Exp. (8) under pressure up to 5 TPa (pink stars), that is superimposed upon the orbital image. The tomography confirms that even such enormous pressure cannot distort the orbitals and so the strength of their covalent bonds is enough to keep the diamond structure²³.

At last, the hit of our work is an orbital tomography – the reconstruction of the form of the orbital by means of the layer-by-layer scan of its radii R versus the covalent radii r_c , which uses the temperature-pressure diagram as microscope. The stress-induced decrement of the covalent radius $\partial r_c(P)$ increases the orbital intersection on the disk-shaped layer $2\pi R(r_c)^2 \partial r_c(P)$ which induces the increment of the melting energy per half an sp^3 covalent bond $k_B \partial T_{tr}(P)/8 = 2\pi \nu R(r_c)^2 \partial r_c(P)$. Then the measurements of the derivative $\partial T_{tr}(P)/\partial r_c(P)$ allow us to profile the orbital via its radii

$$R(r_c) = \frac{1}{4} \sqrt[4]{\frac{k_B \partial T_{tr}(P)}{\pi \nu \partial r_c(P)}}. \quad (8)$$

$R(r_c)$ derived from $T_{tr}(P)$ digitized from red line on the inset of Fig⁴. 4 and $r_c(P)$ calculated from Exp. (7) through the same $\rho(P)$ table²⁴ excellently outline the sp^3 orbital (Fig. 4b).

Thus, the announced atomic constant $\nu = 8.941 \text{ eV/\AA}^3$ obtained from fitting AC has been also confirmed by drawing BC and $T_C(P)$, the calculation of the hysteresis, the melting point and orbital tomography in diamond at ultrahigh pressures. Our discovery qualitatively explains the diagrams of antiferromagnetics⁵⁻¹⁰ not clear for decades. Pressure, holding the transition-cation planes away from the anion planes in NiS, V₂O₃ and RNiO₃ (R = Pr, Nd, Nd_{0.7}La_{0.3}), narrows the e_g - p orbital overlappings, so that T_N lowers and the e_g electrons, which cannot migrate because of antiferromagnetism, gradually become current carriers. The BaVS₃ diagram⁸ become understandable if to take into account that the pressure-induced orbital overlaps in the V-S chains favours to antiferromagnetism which impedes conductance. The linear $T_N(P)$ of the Gd, Pr and Tm orthoferrites⁹ means the fulfillment of Hooke law at their small rare-earth-cation radii, but the more radius in the La orthoferrite⁹ shortens the Fe-O bond and so inflates the $3d$ and $2p$ orbital intersection that causes the lift and nonlinearity of its $T_N(P)$. Expression (6) with the chemical pressure $P_i \sim 1 - y/y_p$ (y_p is a doping index of the paramagnetic composition) instead of P could fit the $T_N(y)$ diagram¹⁰ of Ni_{1-x}S_{1-y}Se_y. The coincidence of the Sm_{0.55}Sr_{0.45}MnO₃ Curie point with the MnO Neel point hints at their same intersection volumes, that is, distinct-type transitions can have their near critical points, then certain substances must pose on the near points of the diagram “*intersection volume–T_c*”, revealing that their phase transitions caused by the orbital overlapping. Although the wave function is smear, the outline of orbital is sharp (Fig. 4b), that is, electron is like a son who was forbidden by his father to leave the yard, but he sometimes leaves and returns; so that chemists, specifying the orbital overlapping, can tailor necessary substance properties without complicated quantum simulations.

References

1. Van der Waals, J. D. The equation of state for gases and liquids. *Nobel Lecture, December 12, 1910*. <https://www.nobelprize.org/prizes/physics/1910/waals/lecture/>.
2. Feng, J. et al. Large linear magnetoresistance in Dirac semimetal Cd₃As₂ with Fermi surfaces close to the Dirac points. *Phys. Rev. B* **92**, 081306(R) (2015).
3. Samatham, S., Barua, S. & Suresh, K.G. Spin-flop quasi-first order transition and putative tricritical point in Gd₃Co. *JMMM* **444**, 439-443 (2017).
4. Eggert, J.H. et al. Melting temperature of diamond at ultrahigh pressure. *Nature Physics* **6**, 40-43 (2010).
5. McWhan, D.B., Marezio, M., Remeika, J. P. & Dernier, P.D. Pressure-temperature phase diagram and crystal structure of NiS. *Phys. Rev. B* **5**, 2552-2555 (1972).
6. Carter, S.A., Rosenbaum, T.F., Lu, M. & Jaeger, H.M. Magnetic and transport studies of pure V₂O₃ under pressure. *Phys. Rev. B* **49**, 7898-7903 (1994).
7. Obradors, X. et al. Pressure dependence of the metal-insulator transition in the charge-transfer oxides RNiO₃ (R = Pr, Nd, Nd_{0.7}La_{0.3}). *Phys. Rev. B* **47**, 12353-12356 (1993).
8. Fazekas, P. et al. Magnetic-field-induced transition in BaVS₃. *Phys. Rev. B* **75**, 035128 (2007).
9. Halasa, N.A., DePasquali, G. & Drickamer, H.G. High-pressure studies on ferrites. *Phys. Rev. B* **10**, 154-164 (1974).

10. Matoba M., Anzai, S. & Fujimori, A. Thermal expansion, thermoelectric power, and XPS study of the non-metal-metal transition in $\text{Ni}_{1-x}\text{S}_{1-y}\text{Se}_y$. *J. Phys. Soc. Jap.* **60**, 4230-4244 (1991).
11. Limelette, P. et al. Universality and critical behavior at the Mott Transition. *Science* **302**, 89-92 (2003).
12. McKenzie, R.N. Similarities between organic and cuprate superconductors. *Science* **278**, 820-821 (1997).
13. Kagawa, F., Miyagawa, & K. Kanoda, K. Unconventional critical behaviour in a quasi-two dimensional organic conductor. *Nature* **436**, 534-537 (2005).
14. J. D. van der Waals, J. D. – Biographical.
<https://www.nobelprize.org/prizes/physics/1910/waals/biographical/>.
15. Anderson, O.L. Iron: beta phase frays. *Science* **278**, 821-822 (1997).
16. Medarde, M. et al. High-pressure neutron-diffraction study of the metallization process in PrNiO_3 . *Phys. Rev. B* **52**, 9248-9258 (1995).
17. Zhou, J.-S. & Goodenough, J.B. Unusual evolution of the magnetic interactions versus structural distortions in RMnO_3 perovskites. *Phys. Rev. Lett.* **96**, 247202 (2006).
18. Abdulvagidov, S.B., Djabrailov, S.Z. & Abdulvagidov, B.S. Nature of novel criticality in ternary transition-metal oxides. *Sci Rep* **9**, 19328 (2019). <https://doi.org/10.1038/s41598-019-55594-w>.
19. Lalitha, G. & Reddy, P.V. Elastic behavior of some manganite-based orthorhombic RMnO_3 ($\text{R} = \text{Sm}, \text{Eu}, \text{Gd}, \text{Dy}$) multiferroics. *JMMM* **320**, 754–759 (2008).
20. Street, R. & Lewis, B. Anomalous variation of Young's modulus of antiferromagnetics at the Neel point. *Nature* **168**, 1036-1037 (1951).
21. Treacy, M.M.J., Ebbesen, T.W. & Gibson, J.M. Exceptionally high Young's modulus observed for individual carbon nanotubes. *Nature* **381**, 678-680 (1996).
22. Pyykko, P. Refitted tetrahedral covalent radii for solids. *Phys. Rev. B* **85**, 035128 (2012).
23. Lazicki, A. et al. Metastability of diamond ramp-compressed to 2 terapascals. *Nature* **589**, 532-535 (2021).
24. Smith, R.F. et al. Ramp compression of diamond to five terapascals. *Nature* **511**, 330-332 (2014).
25. Abdulvagidov, Sh.B., Kamilov, I.K., Aliev, A.M. & Batdalov, A.B. Heat capacity and electric resistance of $\text{Sm}_{0.55}\text{Sr}_{0.45}\text{MnO}_3$ manganite near T_C in a magnetic field of up to 26 kOe: fluctuation effects and colossal magnetoresistance development scenario. *Zh. Éksp. Teor. Fiz.* **123**, 857 (2003) [*JETP* **96**, 757 (2003)].
26. De Teresa, J.M. et al. Magnetic versus orbital polarons in colossal magnetoresistance manganites. *Phys. Rev. B* **65**, 100403(R) (2002).
27. Demko, L. et al. Multicritical end point of the first-order ferromagnetic transition in colossal magnetoresistive manganites. *Phys. Rev. Lett.* **101**, 037206 (2008).
28. Lalitha, G. & Reddy, P.V. Elastic behavior of strontium-doped lanthanum calcium manganites in the vicinity of T_C . *J. Phys. Chem. Solids* **70**, 960–966 (2009).
29. Sommerfeld, A. *Atombau und spektrallinien* (Friedr. Vieweg & Sohn, Braunschweig, 1951).
30. Kurbakov, A.I., Trunov, V.A. & Andre, G. Study of effect isotopic substitution $^{16}\text{O} \rightarrow ^{18}\text{O}$ in $\text{Sm}_{1-x}\text{Sr}_x\text{MnO}_3$ -type ($x = 0.45$ and 0.50) manganites by powder neutron diffraction. *Crystallography Reports* **49**, 899–906 (2004).

Competing interests The author declares no competing interests.

Additional information

Supplementary information The online version contains supplementary material available at <https://doi.org/10.1038/> _____.

Correspondence and requests for materials should be addressed to the author.

Peer review information *Nature* thanks ___ for their contribution to the peer review of this work.

Reprints and permissions information is available at www.nature.com/reprints.

Affiliations Institute of Physics, Dagestan Federal Research Centre of RAS, 94, Makhachkala
367015. Republic of Dagestan.

Table 1. Initial data and fitted parameters in tracing the phase boundaries on Figs. 1 and 3.

	Curve AC	Point B	Line BC	Curve $T_C(P)$
$\mu = 6\mu_B$	■	■	■	■
$a = 0.9775 \text{ \AA}$	■	■	■	■
$V = 226.301 \text{ \AA}^3$	■	■	■	■
$R = a/4$	■	■	■	■
$h_A = 0.027147 \text{ \AA}$	■	■	■	■
$\theta_A = 9.85^\circ$	■	■	■	■
$\theta_C = 8.5^\circ$	■	■	■	■
$E_0 = 25.31 \text{ GPa}$	■	■	■	■
$\nu = 8.941 \text{ eV/\AA}^3$	■	■	■	■
$a_B = 0.97628 \text{ \AA}$	■	■	■	■
$\theta_B = 9.5^\circ$	■	■	■	■
$h_B = 0.0291592 \text{ \AA}$	■	■	■	■

R , h_A , θ_A , θ_C , E_0 and ν are fitted parameters of the curve AC. The tilting angle θ derives from the angle α of the chemical bond $\text{Mn}^{3+}\text{-O}^{2-}\text{-Mn}^{4+}$: $\theta = (\pi - \alpha)/2$. The normal-condition Young's modulus E_0 is in good agreement with values for manganites²⁸. R is about a fourth of the orbital length that is standard for d and p orbitals²⁹. The values of a and V are calculated from the neutron-diffraction data^{18,30}. a_B , θ_B and h_B are fitted parameters of the point B. The values of a_B , θ_A and θ_B are in good consistency with the neutron-diffraction data^{18,30}. And θ_C is in good agreement with θ_{DE} , that is, $\theta_C \approx \theta_{DE}$. All the calculations were carried out in Supplementary Table S1. As seen, the fitted (■) data of AC are initial (■) for BC, B and $T_C(P)$. And the fitted values of B are initial for BC and $T_C(P)$. So, BC is drawn only with the initial data, without fitting. $T_C(P)$ is traced only with fitting the prefactor and power in the pressure-depended Young's modulus $E(P) = 325P^{1/3} + E_0$.

Supplementary Files

This is a list of supplementary files associated with this preprint. Click to download.

- [SupplementaryTableS11.xlsx](#)